ACS APPLIED MATERIALS & INTERFACES

Letter

www.acsami.org

Retaining the 3D Framework of Zinc Sponge Anodes upon Deep Discharge in Zn–Air Cells

Joseph F. Parker,* Eric S. Nelson,† Matthew D. Wattendorf,‡ Christopher N. Chervin, Jeffrey W. Long, and Debra R. Rolison*

Surface Chemistry Branch, Code 6170, U.S. Naval Research Laboratory, Washington, District of Columbia 20375, United States

Supporting Information

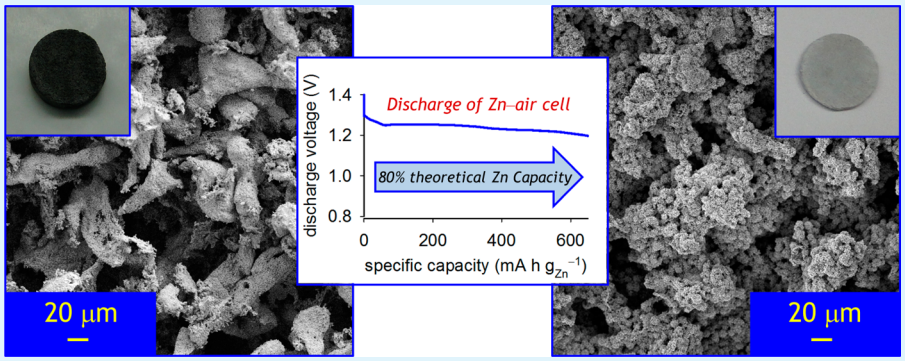

ABSTRACT: We fabricate three-dimensional zinc electrodes from emulsion-cast sponges of Zn powder that are thermally treated to produce rugged monoliths. This highly conductive, 3D-wired aperiodic scaffold achieves 740 mA h g_{Zn}^{-1} when discharged in primary Zn–air cells (>90% of theoretical Zn capacity). We use scanning electron microscopy and X-ray diffraction to monitor the microstructural evolution of a series of Zn sponges when oxidized in Zn–air cells to specific depths-of-discharge (20, 40, 60, 80% DOD) at a technologically relevant rate (C/40; 4–6 mA cm^{-2}). The Zn sponges maintain their 3D-monolithic form factor at all DOD. The cell resistance remains low under all test conditions, indicating that an inner core of metallic Zn persists that 3D-electrically wires the electrode, even to deep DOD.

KEYWORDS: *zinc, zinc–air, batteries, morphology, energy, three-dimensional architecture*

Zinc-based batteries offer many appealing characteristics, including low-cost components, water-based electrolytes, and high energy density, yet their broader applicability has been limited by suboptimal performance of the Zn anode, which undergoes complex chemical and electrochemical reactions during operation.[1−6] As Zn is oxidized, soluble zincate intermediates (e.g., $Zn(OH)_4^{2-}$) are generated that, upon supersaturation, precipitate and dehydrate to poorly conducting ZnO[7−9] (eq 1–3).

$$Zn(s) \rightarrow Zn^{2+} + 2e^- \text{ (oxidation)} \quad (1)$$

$$Zn^{2+} + 4OH^-(aq) \rightarrow Zn(OH)_4^{2-}(aq) \text{ (complexation)} \quad (2)$$

$$Zn(OH)_4^{2-}(aq) \rightarrow ZnO(s) + H_2O + 2OH^-(aq) \text{ (passivation)} \quad (3)$$

Zinc electrodes for alkaline batteries (e.g., Zn–MnO_2, Ni–Zn, Ag–Zn, and Zn–air) are commonly constructed from slurries or pastes that comprise Zn powder, gelling agents, and binders. The ad hoc nature of powder-composite electrodes often leads to electronically isolated Zn particles once ZnO coats nearby surfaces, thereby terminating discharge at 50–60% utilization, well below the theoretical Zn specific capacity (820 mA h g_{Zn}^{-1}).[10,11] Disruption of electronic continuity also frustrates subsequent attempts to recharge the Zn/ZnO electrode because the charging current is redirected to localized reaction sites, a condition that is ripe to breach the critical current density that promotes formation of electrical short-inducing dendrites.[12]

We recently demonstrated that Zn electrodes redesigned as sponge-like porous architectures achieve high specific capacity in primary Zn–air cells (>85% Zn utilization) and dendrite-free cycling to moderate capacity in Ag–Zn cells (up to 188 mA h g_{Zn}^{-1}).[13−15] High capacity and minimized dendrite growth are realized because of the innate structural characteristics of Zn sponges: well-wired networks of metallic Zn that facilitate both long-range electronic conductivity and more uniform current distribution in concert with confined void volume that constrains the products of Zn/ZnO redox within the 3D electrode structure.

Received: August 6, 2014
Accepted: October 28, 2014
Published: October 28, 2014

Table 1. Parameters for Electrochemical Discharge Tests of Zn−air Cells

experiment	discharge rate	depth-of-discharge (%)	specific capacity (mA h g_{Zn}^{-1})	average discharge voltage (V)	specific energy (W h kg_{Zn}^{-1})	$R_{cell,initial}$ [c] (Ω cm^{-2})	$R_{cell,post-discharge}$ [c] (Ω cm^{-2})
3D Zn-20[a]	C/40	20	164	1.25	205	1.31	1.22
3D Zn-40[a]	C/40	40	328	1.23	404	1.20	1.56
3D Zn-60[a]	C/40	60	492	1.21	597	1.79	2.28
3D Zn-80[a]	C/40	80	656	1.24	812	1.21	0.79
3D Zn-full[b]	C/15	91	743	1.19	882	1.93	0.75
commercial[b]	C/15		failed immediately (<30 s)				
commercial	C/40	69		1.11		0.65	3.96

[a]These data are derived from one set of 20−40−60−80% DOD, but two additional replicate series run at different times yielded comparable results. [b]Cell allowed to discharge to 0.9 V cutoff. [c]R_{cell} (Ω cm^{-2}) is calculated from the cell resistance divided by the geometric area of the full cell.

In the present report, we explore how the microstructure of the Zn sponge evolves during discharge in primary Zn−air cells by taking a series of Zn sponges to controlled depths-of-discharge, DOD (0−80% in 20% increments) and examining their physicochemical structure post−discharge. We assess the ability of the Zn sponge to (i) support uniform deposition of the discharge end-product, ZnO; (ii) maintain a monolithic form factor; and (iii) retain low cell resistance, even to deep levels of discharge. The results obtained from this systematic study of the Zn sponge microstructure as discharged in 6 M KOH will inform design optimization for the next generation of 3D Zn architectures, as well as other performance factors, such as the impact of electrolyte additives on Zn morphology.

Zinc sponges are fabricated as described previously[14] by forming an emulsion of Zn powder, water, decane, sodium dodecyl sulfate, and carboxymethylcellulose,[16] and casting the emulsion in a 1.15 cm−diameter cylindrical mold. After drying and releasing the Zn sponges from their molds, they are heated to 410 °C under flowing Ar and then to 665 °C in static air, a procedure that sinters the Zn particles beneath a stabilizing coating of ZnO to form mechanically rugged, 1−3 mm thick monoliths. A subsequent bulk electrolysis step in 6 M KOH is used to reduce the ZnO shell and generate metallic Zn^0 sponges.[14]

Primary Zn−air cells are constructed within a cylindrical nylon casing, where the all-metal Zn sponge anode (dipped in a gel electrolyte of 6 M KOH/poly(acrylic acid)[17]) is placed atop a Sn current collector.[18] A Celgard 3501 separator is placed between the Zn sponge and a commercially sourced air cathode (E4; Electric Fuels, Inc.), which is contacted to the positive terminal via nickel-mesh. Multiple series of Zn−air cells were galvanostatically discharged at a C/40 rate (corresponding to 20.5 mA g_{Zn}^{-1}) to fixed depths-of-discharge (20, 40, 60, and 80% of the theoretical Zn specific capacity, Table 1). The resulting discharge curves are relatively flat with average voltages maintained at the >1.2 V characteristic of Zn−air cells (Figure 1).

Following discharge, the Zn sponges are harvested from the cell, water-rinsed to remove electrolyte, and dried under vacuum at room temperature. Visual inspection of the discharged Zn sponges shows the effects of ZnO accumulation, with the color of the sponges progressing from dark metallic gray toward lighter gray with increasing DOD (Figure 1 insets), consistent with an increase in ZnO (a white compound) on the surfaces of the Zn sponge. The discharged sponges remain monolithic and mechanically robust enough to handle, even after the excursion to 80% DOD, challenging the too-common expectation that the electrodissolution inherent to Zn oxidation in alkaline electrolyte ultimately disintegrates the solid

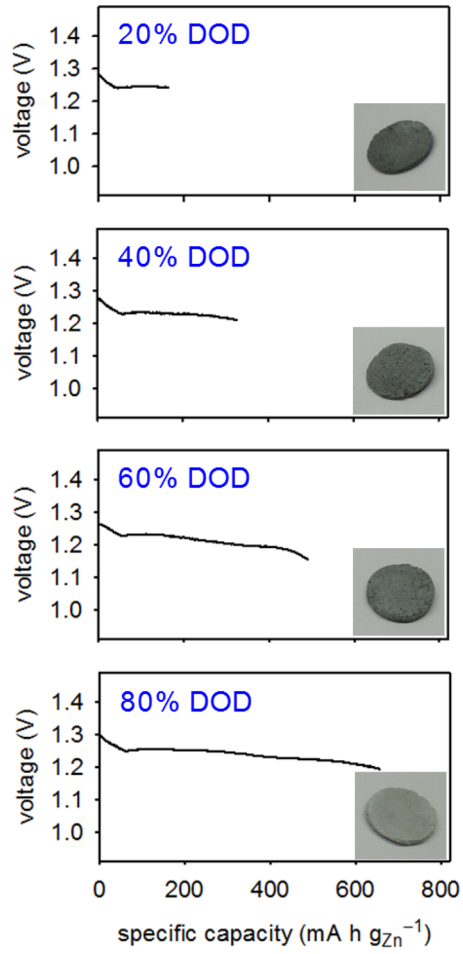

Figure 1. Series of Zn−air cells galvanostatically discharged at a C/40 rate to fixed depths-of-discharge (20, 40, 60, and 80% of the theoretical Zn specific capacity). Insets: photographs of water-rinsed and vacuum dried post−discharged Zn sponges revealing retention of their monolithic forms, with a color change from dark to lighter gray as ZnO progressively accumulates upon deeper DOD.

electrode and that a high-surface-area 3D Zn structure should be even more susceptible.

Scanning electron microscopy (SEM) was used to examine the post−discharge microstructure at the separator-facing boundary and in the cross-sectional interior of the sponge. The porous 3D structure is retained at all levels of discharge. The surfaces of pre−discharged Zn sponges exhibit compact platelike features at micrometer resolution; as discharge progresses, needlelike crystals of ZnO form, first in islands

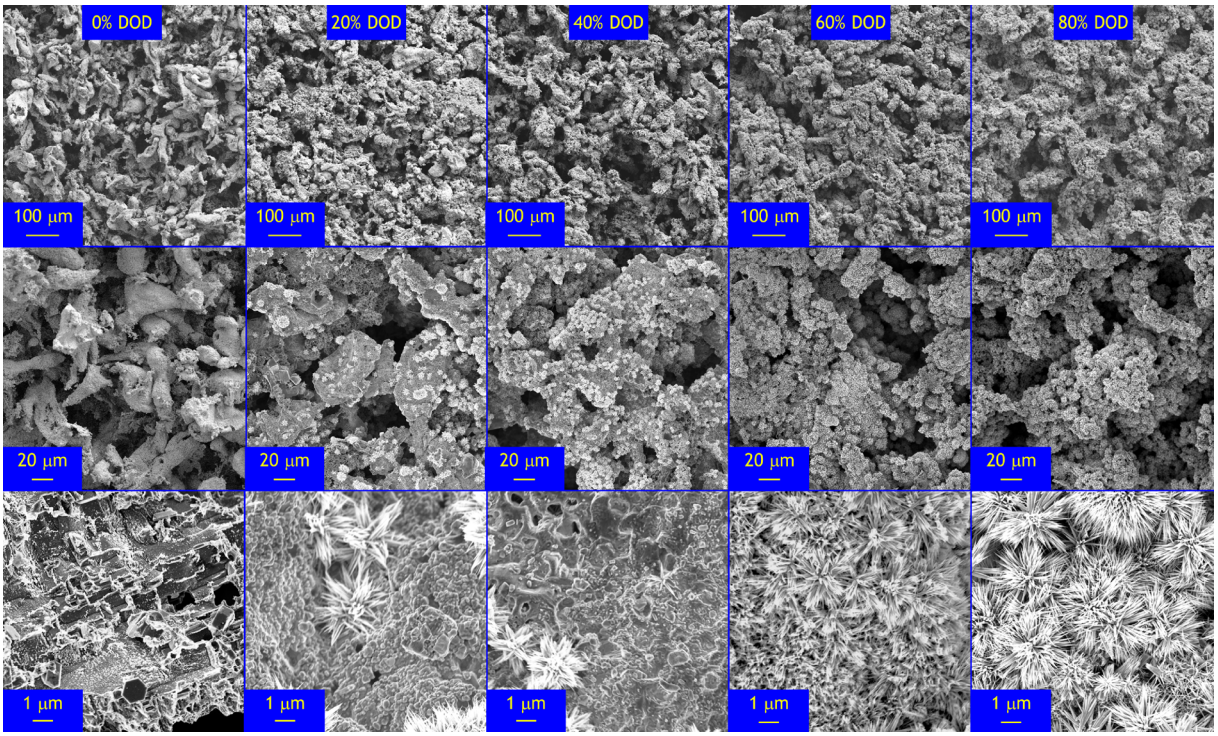

Figure 2. Scanning electron micrographs of the post−discharged microstructure at the separator-facing boundary of the discharged Zn sponge anodes. The porous 3D structure is retained at all levels of discharge. As discharge progresses, needlelike crystals of ZnO form, first in islands that eventually coalesce to uniform carpetlike deposits throughout the electrode structures.

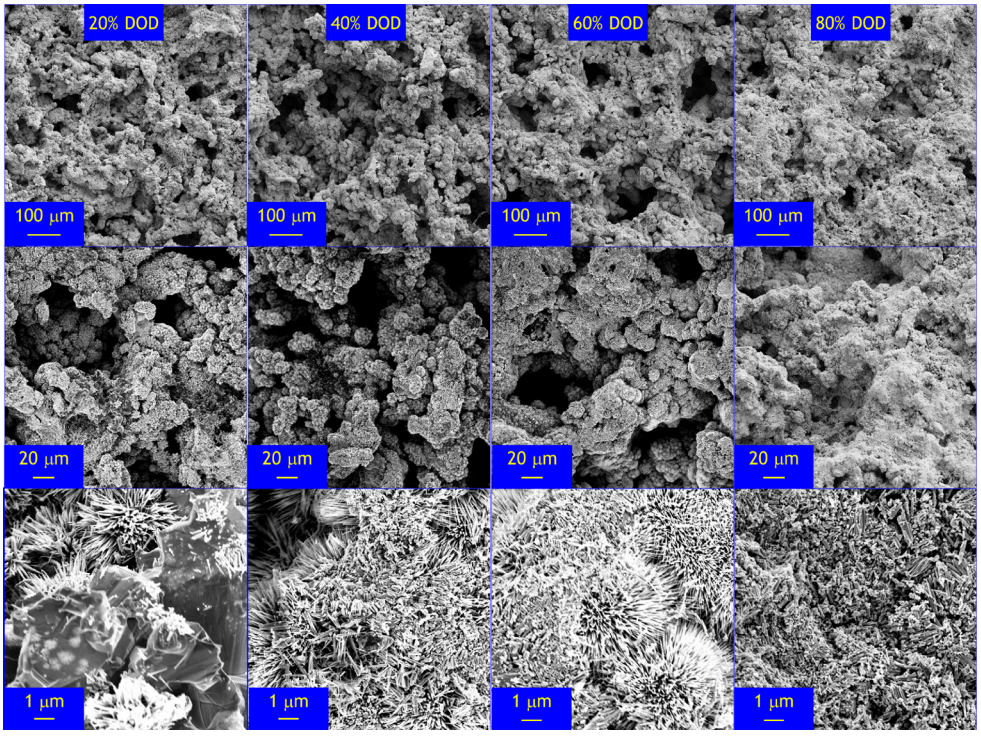

Figure 3. Scanning electron micrographs of the interior of the discharged Zn sponge anodes, which sport denser accumulations of ZnO deposits than observed at the exterior (see Figure 2) and arise from enhanced precipitation of ZnO within the confined free volume of the interior. The open porosity and interconnection of the sponges particles are maintained throughout all depths-of-discharge.

that eventually coalesce to uniform carpetlike deposits at all of the inner and boundary surfaces of the electrode structure, as seen in Figure 2 (boundary) and Figure 3 (interior). The interior of the sponge sports a denser accumulation of ZnO deposits than observed at the exterior, which we attribute to enhanced precipitation of ZnO within the confined free volume of the interior (see Figure S1 in the Supporting Information for replicate data).

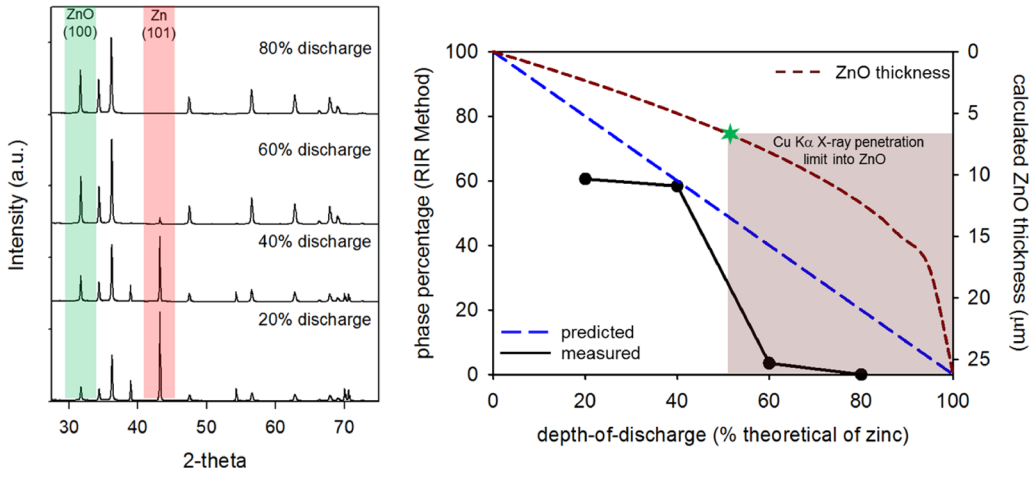

Figure 4. (left) X-ray diffraction of the post−discharged Zn sponge electrodes at 20−80% DOD. (right) Phase percentage of ZnO as a function of the depth of discharge as calculated using the reference intensity ratio, RIR (black line). The measured RIR values are compared to the predicted RIR values (dotted blue line). The RIR calculation consistently inflates the percentage of ZnO present in the discharged anodes. The disparity is attributed to the growing thickness of ZnO on the backbone of the metallic Zn architecture (dotted red line) and the attenuation of the Zn reflections due to the penetration-depth limitations of Cu Kα X-rays.

We estimate that the discharge capacity required to achieve the solubility limit of potassium zincate in 6 M KOH[8] within the total interior volume of 0.16 mL for a 1.7 mm−thick porous sponge is 17 mA h g_{Zn}^{-1} (2% depth-of-discharge).[19] This calculation does not account for local effects of volume confinement, tortuosity, or dynamic mass-transport conditions. Previous experimental and modeling studies[20,21] revealed that precipitation within porous objects occurs preferentially within small pores relative to bulk solution; thus in the present case, the discharge capacity required to initiate precipitation of ZnO within our Zn sponge is likely less than that derived in the simple calculation described above. To gauge the efficacy of capturing discharged Zn as ZnO, the mass of each Zn sponge was obtained before and after discharge and compared with the predicted mass change associated with full conversion to ZnO at each specific DOD (see Table S2 in the Supporting Information). For example, at 80% DOD (80% conversion of Zn to ZnO), the predicted mass increase is 19.6%, whereas the measured value is 21.6%. This close agreement further confirms that ZnO within the 3D sponge structure is substantially confined to the surfaces of the interconnected Zn electrode rather than dispersed throughout the cell volume as solvated zincate species.

The conversion of Zn to ZnO was assessed by ex situ X-ray diffraction (XRD; Rigaku Smartlab, Cu−Kα) for the post−discharged and water-rinsed Zn sponge electrodes (Figure 4). The reference intensity ratio (RIR) method[22] was used to correlate the amount of Zn converted to ZnO for each DOD by ratioing the intensity of the most-intense reflection for ZnO to that of the most-intense reflection for Zn. The RIR calculations consistently inflate the percentage of ZnO present in the discharged Zn anodes, a disparity that is attributed to the growing thickness of ZnO on the backbone of the metallic Zn architecture. The limitations of the RIR method for this calculation are a consequence of the penetration depth, x_e, of X-rays from the Cu−Kα source (8.046 keV)

$$x_e = \frac{\sin\Omega\sin(2\theta - \Omega)}{\mu[\sin\Omega + \sin(2\theta - \Omega)]}$$

where Ω is the incident angle, 2θ is the angle of diffraction, and μ is the linear absorption coefficient of ZnO under Cu−Kα radiation (calculated to be 274 cm^{-1}).[23,24] The calculated penetration depth of Cu−Kα X-rays into ZnO at 2θ = 43° (101),[25] the most intense reflection for Zn metal, is 6.7 μm. As the discharge of the Zn−air cell progresses and ZnO accumulates at the surfaces of the Zn sponge anode, the ZnO film thickness increases as plotted in Figure 4 (see the Supporting Information for derivation). The surface thickness of ZnO is calculated to reach 6.7 μm at ∼50% DOD, thereby attenuating Zn (101) reflectivity for sponges discharged to ≥50% DOD. The overestimation of ZnO thickness at ≥50% DOD further supports the hypothesis that ZnO is confined to the surfaces of the Zn backbone in the sponge. To appropriately distinguish the Zn phase beneath its oxide shell requires X-ray photons with energy >21 keV.

The presence at the Zn surfaces of semiconducting ZnO (which has a reported conductivity spanning a broad range from 1×10^{-10} to 1×10^{-3} S cm^{-1})[26,27] may introduce additional resistance within the electrode structure as discharge progresses. Yet, when we discharge Zn−air cells containing 3D Zn sponge anodes, the total cell resistance remains low (∼1 Ω cm^{-2}) even after discharge at high rates (C/15; 9.3 mA) and to high depths-of-discharge (743 mA h g_{Zn}^{-1}; 91% DOD). When commercial Zn−air cells are subjected to similar tests, but discharged at a slower rate (C/40 because the C/15 rate tolerated by 3D Zn−air cells is too demanding), cell resistance increased ∼6-fold from 0.65 Ω cm^{-2} in the as-received state to 3.96 Ω cm^{-2} after exhaustive discharge (reaching only ∼69% DOD; see Figure S3 in the Supporting Information). We attribute the relative invariance in resistance during discharge for cells based on our Zn sponge anodes to the retention of the inner wiring of metallic Zn within the sponge architecture thereby ensuring that long-range electron conduction is maintained throughout discharge. We attribute minor fluctuations in resistance (±100s of mΩ) to cell-to-cell variations such as electrolyte management or electrode mass differences (see Figure S2 and Table S1 in the Supporting Information for replicates). In contrast, the suboptimal particle−particle connectivity characteristic of the powder-composite Zn anode

dx.doi.org/10.1021/am505266c | ACS Appl. Mater. Interfaces 2014, 6, 19471−19476

in the commercial cell creates opportunities for increasing internal resistance during discharge.

The results presented herein are derived from multiple single-discharge tests, but our key findings highlight performance characteristics of Zn sponge architectures that will enable high-performance rechargeable Zn-based batteries. Uniform deposition of discharge products at Zn surfaces within the sponge architecture and retention of low internal resistance, even to deep DOD, should promote uniform reduction of ZnO and minimize the growth of short-inducing Zn dendrites upon extensive charge−discharge cycling. The persistent mechanical ruggedness and monolithicity of the Zn sponge will sustain the structure under challenging conditions. The long-term goal for a redesigned Zn electrode is its implementation into rechargeable Zn−air cells. The Zn sponge electrodes described herein, along with our concurrent efforts on pulse-power−enabled carbon nanofoam air cathodes,[17,28] are but two breakthroughs en route to that goal. We have demonstrated dendrite-free charge−discharge cycling to modest DOD (20% of theoretical Zn utilization) in symmetric Zn/ZnO and Ag−Zn cells,[14] and ongoing experiments are focused on incorporating efficient oxygen-evolution catalysts into air cathodes and constructing prototype rechargeable Zn−air cells.

■ ASSOCIATED CONTENT

Supporting Information

Derivation of the plot of ZnO film thickness as a function of depth-of-discharge, electrochemical impedance spectroscopy, table of mass changes during discharge, and replicate data. This material is available free of charge via the Internet at http://pubs.acs.org.

■ AUTHOR INFORMATION

Corresponding Authors

*(JFP) E-mail: joseph.parker@nrl.navy.mil. Phone: (202) 767-0219.

*(DRR) E-mail: rolison@nrl.navy.mil. Phone: (202) 767-3617.

Notes

The authors declare no competing financial interest.

†Pathways student

‡Student volunteer

■ ACKNOWLEDGMENTS

This work was supported by the U.S. Office of Naval Research. J.F.P. acknowledges a Jerome and Isabella Karle Distinguished Scholar Fellowship from the U.S. Naval Research Laboratory.

■ REFERENCES

(1) Linden, D. Zinc/Air Cells. In *Handbook of Batteries*, 2nd ed.; McGraw-Hill: New York, 1984; Chapter 13.

(2) McBreen, J. Rechargeable Zinc Batteries. *J. Electroanal. Chem.* **1984**, *168*, 415−432.

(3) McLarnon, F. R.; Cairns, E. J. The Secondary Alkaline Zinc Electrode. *J. Electrochem. Soc.* **1991**, *138*, 645−656.

(4) Li, Y.; Dai, H. Recent Advances in Zinc−Air Batteries. *Chem. Soc. Rev.* **2014**, *43*, 5257−5275.

(5) Minakshi, M.; Appadoo, D.; Martin, D. E. The Anodic Behavior of Planar and Porous Zinc Electrodes in Alkaline Electrolyte. *Electrochem. Solid-State Lett.* **2010**, *13*, A77−A80.

(6) Wang, K.; Pei, P.; Ma, Z.; Xu, H.; Li, P.; Wang, X. Morphology Control of Zinc Regeneration for Zinc−Air Fuel Cell and Battery. *J. Power Sources* **2014**, *271*, 65−75.

(7) Dirkse, T. P. The Behavior of the Zinc Electrode in Alkaline Solutions. *J. Electrochem. Soc.* **1981**, *128*, 1412−1415.

(8) Dirkse, T. P. Aqueous Potassium Hydroxide as Electrolyte for the Zinc Electrode. *J. Electrochem. Soc.* **1987**, *134*, 11−13.

(9) Arise, I.; Kawai, S.; Fukunaka, Y.; McLarnon, F. R. Coupling Phenomena Between Zinc Surface Morphological Variations and Ionic Mass Transfer Rate in Alkaline Solution. *J. Electrochem. Soc.* **2013**, *160*, D66−D74.

(10) Harting, K.; Kunz, U.; Turek, T. Zinc−air Batteries: Prospects and Challenges for Future Improvement. *Z. Phys. Chem.* **2012**, *226*, 151−166.

(11) Zhang, X. G. Fibrous Zinc Anodes for High Power Batteries. *J. Power Sources* **2006**, *163*, 591−597.

(12) Oxley, J. E.; Fleishmann, C. W. *First, Second, and Third Quarterly Reports for the Improvement of Zinc Electrodes for Electrochemical Cells*; NASA Technical Documents N66−13568, N66−16956, and N66−26870; National Aeronautics and Space Administration: Washington, D.C., 1965−1966.

(13) Rolison, D. R.; Parker, J. F.; Long, J. W. Zinc Electrode Material for Zinc−Air Batteries. U.S. Pat. Appl. Publ. U.S. 20140147757 A1, May 29, 2014.

(14) Parker, J. F.; Chervin, C. N.; Nelson, E. S.; Rolison, D. R.; Long, J. W. Wiring Zinc in Three Dimensions Re-Writes Battery Performance—Dendrite-Free Cycling. *Energy Environ. Sci.* **2014**, *7*, 1117−1124.

(15) Parker, J. F.; Pala, I. R.; Wattendorf, M. D.; Rolison, D. R.; Long, J. W. Three-Dimensional Zinc Electrode Architectures for Rechargeable Alkaline Batteries. In *Proceedings of the 46th Power Sources Conference*; Orlando, FL, June 9−12, 2014; National Technical Information Service: Springfield, VA, 2014; Vol. *34*, pp 517−519.

(16) Drillet, J.-F.; Adam, M.; Barg, S.; Herter, A.; Koch, D.; Schmidt, V.; Wilhelm, M. Development of a Novel Zinc/Air Fuel Cell with a Zn Foam Anode, a PVA/KOH Membrane, and a MnO_2/SiOC-Based Air Cathode. *ECS Trans.* **2010**, *28*, 13−24.

(17) Chervin, C. N.; Long, J. W.; Brandell, N. L.; Wallace, J. M.; Kucko, N. W.; Rolison, D. R. Redesigning Air Cathodes for Metal−Air Batteries Using MnO_x-Functionalized Carbon Nanofoam Architectures. *J. Power Sources* **2012**, *207*, 191−198.

(18) Bonnick, P.; Dahn, J. R. A Simple Coin Cell Design for Testing Rechargeable Zinc−Air or Alkaline Battery Systems. *J. Electrochem. Soc.* **2012**, *159*, A981−A989.

(19) The porosity of our Zn sponges is 82% ± 1.5%, from which we can derive the volume of the pores, V_p, from the measured geometric volume. The molar solubility, $s_{zincate}$, of potassium zincate in 6 M KOH is ~0.5 M $K_2Zn(OH)_4$.[8] The mass of Zn, m_{Zn}*, required for discharge to achieve $s_{zincate}$ is therefore $V_p s_{zincate} MW_{Zn}$. The corresponding discharge capacity is therefore m_{Zn}^*/m_{Zn}^{tot} or 2% (17 mA h g_{Zn}^{-1}).

(20) Rad, M. N.; Shokri, N.; Sahimi, M. Pore-Scale Dynamics of Salt Precipitation in Drying Porous Media. *Phys. Rev. E* **2013**, *88*, 032404−1−032404−5.

(21) Mao, Z.; White, R. E. Mathematical Modeling of a Primary Zinc/Air Battery. *J. Electrochem. Soc.* **1992**, *139*, 1105−1114.

(22) Hubbard, C. R.; Evans, E. H.; Smith, D. K. The Reference Intensity Ratio, I/I_c, for Computer Simulated Powder Patterns. *J. Appl. Cryst.* **1976**, *9*, 169−174.

(23) Sarkar, A.; Chakrabarti, M.; Bhowmick, D.; Chakrabarti, A.; Ray, S. K.; Rafaja, D.; Sanyal, D. Defects in 6 MeV H^+ Irradiated Hydrothermal ZnO Single Crystal. *J. Phys.: Condens. Matter* **2013**, *25*, 385501−385508.

(24) Prince, E. *International Tables for Crystallography (Mathematical, Physical and Chemical Tables)*, 3rd ed.; Wiley: New York, 2004; Vol. *100*.

(25) Cho, S.; Jang, J.-W.; Lee, J. S.; Lee, K.-H. Room Temperature Synthesis and Optical Properties of Small Diameter (5 nm) ZnO Nanorod Arrays. *Nanoscale* **2010**, *2*, 2199−2202.

(26) Bonasewicz, P.; Hirschwald, W.; Neumann, G. Influence of Surface Processes on Electrical, Photochemical, and Thermodynamical Properties of Zinc Oxide Films. *J. Electrochem. Soc.* **1986**, *133*, 2270−2278.

(27) Colak, H.; Turkoglu, O. Studies on Structural and Electrical Properties of Copper-Doped Zinc Oxide Powders Prepared by a Solid

State Method at High Temperatures. *Mater. High Temp.* **2012**, *29*, 344−350.
(28) Long, J. W.; Chervin, C. N.; Kucko, N. W.; Nelson, E. S.; Rolison, D. R. Dual-Function Air Cathode for Metal−Air Batteries with Pulse-Power Capability. *Adv. Energy Mater.* **2013**, *3*, 584−588.